Accepted Manuscript

Influence of tab debonding on measured stiffness evolution in Compression-Compression and Tension-Compression fatigue testing of short gauge length coupons

R.D.B. Sevenois, D. Garoz, F.A. Gilabert, C. Hochard, W. Van Paepegem

PII: S0266-3538(18)33092-6

DOI: https://doi.org/10.1016/j.compscitech.2019.05.007

Reference: CSTE 7650

To appear in: *Composites Science and Technology*

Received Date: 18 December 2018

Revised Date: 18 March 2019

Accepted Date: 3 May 2019

Please cite this article as: Sevenois RDB, Garoz D, Gilabert FA, Hochard C, Van Paepegem W, Influence of tab debonding on measured stiffness evolution in Compression-Compression and Tension-Compression fatigue testing of short gauge length coupons, *Composites Science and Technology* (2019), doi: https://doi.org/10.1016/j.compscitech.2019.05.007.

Influence of Tab Debonding on Measured Stiffness Evolution in Compression-Compression and Tension-Compression Fatigue Testing of Short Gauge Length Coupons

R.D.B. Sevenois[a,b,*], D. Garoz[a,b], F.A. Gilabert[a,b], C. Hochard[c], W. Van Paepegem[a]

[a] *Department of Materials, Textiles and Chemical Engineering, Faculty of Engineering and Architecture, Ghent University, Technologiepark Zwijnaarde 46, B-9052 Zwijnaarde, Belgium*
[b] *SIM Program M3Strength, Technologiepark Zwijnaarde 48, B-9052 Zwijnaarde, Belgium*
[c] *Laboratoire de Mécanique et d'Acoustique, 4 impasse Nikola Tesla, 13013 Marseille, France*

Abstract

Short gauge length coupons of plain woven Carbon/Epoxy with layup $[\#(0/90)]_{24}$ and $[\#(45/-45)]_{24}$ are subjected to Compression-Compression and Tension-Compression fatigue loading at several stress levels. Inspection of the gauge length with Digital Image Correlation (DIC) allows measurement of the strain field. The hysteresis loops, axial and shear stiffness as a function of the number of cycles are obtained from the strain field and measured load. For most of the tests a general degradation of the specimen stiffness is observed. For the coupons subjected to uniaxial Compression-Compression with layup $[\#(45/-45)]_{24}$, however, a 17% stiffness increase is seen during the first 10^4 cycles. Post-mortem inspection revealed that the aluminium tabs of the coupons, to facilitate load introduction from the clamps, had partially debonded during testing. A 3D finite element analysis of the coupons including tabs is carried out to investigate the phenomena. The degradation of the tab-coupon bond is modelled using contact with debond capability. This confirmed that tab debonding is responsible for significantly altering the stress state in the (short) gauge section which results in an apparent stiffening of the sample during fatigue loading. Hereby, the authors offer a new explanation for stiffness increase of composite coupons in fatigue tests. For future tests it is shown that quantification of tab debonding is necessary to provide a decisive answer about the experimental boundary conditions in the gauge section of the coupon.

Keywords: A. Laminates, A. Polymer-matrix composites (PMCs), B. Fatigue, B. Mechanical Properties

1. Introduction

The mechanical properties (stiffness and strength) of unidirectional (UD) composite materials are usually obtained through standardized tensile or compressive testing of small coupons [1, 2]. Because a UD composite ply is transverse isotropic, the longitudinal, transverse and shear properties need to be independently determined. In the test, a particular deformation mode is achieved through intelligently changing the so-called layup of the coupons. For example, the longitudinal tensile stiffness strength is tested with a [0] layup, while the shear stiffness and strength can be obtained using a configuration where the plies are rotated at 45 degree, e.g. $[+45/-45]_{2s}$.

*Corresponding author
Email address: ruben.sevenois@ugent.be (R.D.B. Sevenois)
URL: composites.ugent.be (R.D.B. Sevenois)

To obtain reliable experimental results one has to be vigilant. The specimen shape preferably allows sufficient decay of the stress concentrations to produce a uniform strain field in the test region. The specimen has to be carefully produced and tabs (if there are any) need to be properly attached. For the measurement of strain in the test section, one has to verify that strain gauges are not detaching, extensometers do not show slip and optical tracking techniques (e.g. Digital Image Correlation (DIC)) are properly calibrated.

Failure to recognize mistakes in the test setup can have significant implications for the results. For example, slippage of the extensometer during testing can lead to artificial stiffening or softening. Misalignment of the plies during layup of the layers could initiate premature failure. Also specimen buckling can, if not detected during compressive testing, cause premature failure and incorrect strain measurements.

Because composite materials can, under certain loading conditions, exhibit severe non-linear behaviour it is sometimes difficult to distinguish measurement/experiment errors from true material behaviour. It is well known, for example, that realignment of fibers with respect to the loading direction can cause a stiffness increase [3, 4]. Also, it is known that carbon fibers can show intrinsic stiffening upon stretching [5].

The previous phenomena of stiffening and strengthening behaviour mainly concern static testing. For fatigue testing it is generally accepted that the material stiffness should remain stable or degrade over time. Sometimes, however, it is observed that the measured material stiffness (momentarily) increases rather than decreases. Shokrieh and Lessard [3, 4] documented an 8% to 13% stiffness increase for Uni-Directional (UD) Carbon/Epoxy coupons subjected to Tension-Tension (TT) fatigue in the longitudinal or transversal fiber direction. Brunbauer et al. [6] showed a steady increase in stiffness up to about 1% towards the end of life of UD Carbon/Epoxy coupons with the off-axis layup $[45]_4$. Recently, Stelzer et al. [7] showed an initial stiffness increase of about 6% in the first 10^3 cycles of UD Glass/Epoxy coupons with layup $[0/45/90/-45/0]_{2s}$ subjected to TT fatigue at a stress ratio, $R = 0.1$.

In the mentioned research multiple causes for this stiffness increase are proposed. Shokrieh and Lessard [3, 4] proposed that the increase is caused by the realignment of some fibers with the loading direction. Brunbauer et al. [6] indicated that slippage of the extensometer, due to realignment of the off-axis fibers with the loading direction, led to a false increasing strain amplitude. The latter is supported by measurements of the coupon stiffness from actuator force and displacement which did not show a stiffness increase. Stelzer et al. [7] do not discuss the stiffness increase.

In this work, stiffness increase is measured during testing of short gauge length coupons from plain woven Carbon/Epoxy with layup $[\#(45/-45)]_{24}$ in Compression-Compression (CC) and Tension-Compression (TC) fatigue. With respect to the stiffness at the beginning of loading, the stiffness increases about 17% in the first 10^4 cycles before degrading until final failure. Also, coupons with layup $[\#(0/90)]_{24}$ are tested under CC and TC fatigue loading. However, no significant stiffness increase is observed for the latter.

When considering the aforementioned reasons for stiffness increase it is noted that, while they are generally agreed upon for tensile loading, they are not valid under compression loading. In fact, under compression, fibers are expected to buckle or deviate from the load direction rather than align with it. The reasons mentioned in literature can thus not be used as an explanation for this phenomenon.

Post-mortem inspection of the specimens, however, showed that (partial) tab debonding had occurred. For long gauge length samples, tab debonding is not expected to influence the stress/strain distribution in the gauge section. In

this case, however, a short gauge length is used in order to avoid buckling in compression. An unfortunate consequence is that this results in a non-uniform stress state in the gauge section. It is therefore hypothesized that partial debonding of tabs can influence the boundary conditions in the gauge section and, as a result, change the local stress/strain distribution which gives an apparent stiffness increase. Whether this hypothesis is valid has significant implications for future short gauge length tests. Including tab debonding as damage phenomenon or avoiding it by selecting specific adhesives can become necessary.

In this work the effect of tab debonding in combination with a short gauge length on the compressive and tensile-compressive fatigue behaviour of $[\#(0/90)]_{24}$ and $[\#(45/-45)]_{24}$ laminates is shown. This is done by first showing an overview of the experimental evidence of the phenomena. The amount of stiffening, morphology of the hysteresis loops and shape, size of the tab debond area are laid out. The qualitative analysis of the influence of the phenomena is then performed numerically. A coupon including tabs, clamp restriction, tab debonding and nonlinear behaviour of the material is modelled using Finite Element Analysis (FEA). From the model, the strain and stresses are extracted from specific nodes and reference points in a similar way as the manner in which the strain and stress are obtained during the experiments. The resulting stress-strain behaviour and simulated stress/strain distribution in the gauge sections are compared to one-another.

In Section 2 the experimental program and data-acquisition are given. Then, the fatigue test results are given in Section 3. This is followed by the virtual test campaign in Section 4. Section 5 contains a discussion and conclusions.

2. Experimental program

Test coupons with layup $[\#(45/-45)]_{24}$ were manufactured from laminated plates of plain woven Carbon/Epoxy material, "TR3110 360GMP", supplied by Mitsubishi Chemical Corp. To allow recording of the gauge section with cameras for the use of Digital Image Correlation (DIC), the gauge section of the coupon must be free from visual obstruction. DIC is favoured over the classical extensometer because it does not suffer from slipping and allows to capture a strain field rather than a single strain value. Therefore, it was decided to use a coupon design with unsupported gauge length as depicted in ASTM D3410 [1].

2.1. Specimen design and measurement setup

The laminate is 5.7 mm thick. Considering the possible decrease of laminate stiffness by 50% from fatigue degradation, a relatively short gauge length of 25 mm was taken to prevent buckling before final failure [1, 8]. Rectangular aluminium tabs with a thickness of 1.8 mm were used. aluminium was preferred over Glass/Epoxy for several reasons. First, in the experience of the laboratory, aluminium provides a better contact between the clamp and tab surface because the clamp surface, which is roughened, can plastically deform the contact surface. Second, there is no risk of delamination of the layers for the tabs themselves when the final specimen dimensions are cut using a water jet. Third, aluminium allows a more precise production of tab shape which allows to achieve a straight tab end more easily [9] and aids to achieve parallel tab surfaces on each end of the specimen which improves alignment. The tabs were bonded to the plates using Loctite 480 cyanocrylate adhesive and the coupons were subsequently cut from the plates using

water jet cutting. On the coupon surface, a speckle pattern was applied such that surface strains can be identified using DIC. The dimensions of the coupons are shown in Figure 1.

The specimens were subjected to CC and TC fatigue load at several fractions of the static strength and stress ratios $R = 10$ and $R = -1$ on an Instron 100 kN Hydraulic test bench. Before the experimental work was started, the clamps were carefully aligned using a dedicated Instron alignment kit. This was done to avoid premature buckling of the specimen due to clamp misalignment. The pressure on the hydraulic clamps was maintained at 80 bar. Other than the applied load and actuator displacement, which were obtained from the test bench, a single camera positioned perpendicular to the sample surface was used to record the speckle pattern. With one camera the in-plane strains on the surface can be captured. Normally, a 3D camera system with 2 cameras is preferred because it allows to calculate the out-of-plane movement of the investigated surface. It was decided, however, to use the second camera to visualize the side of the specimen to track ply delaminations. In Figure 2 the position of the cameras with respect to the specimen is illustrated. Figure 3 shows a specimen between clamps.

The camera, a PtGrey Grasshopper 3, has a 5 MP sensor and a maximum frame rate of 75 fps. The high frame rate of the camera in combination with a fatigue frequency of 3 Hz allows to capture the strain field at 25 intervals in a single load cycle. This is sufficient to capture the strain field hysteresis loop in a qualitative way without the need to interrupt the fatigue test. With this setup unique information about the longitudinal and transverse local strains as well as the strain pattern is obtained. Important with these measurements is synchronization between cameras and the analog force signal. At test frequencies of 3 Hz, a delay between the measurement of the strain signal and the images taken by the camera of only 15 ms can cause more than 3% deviation between the actual and measured stiffness. For this reason, an in-house developed system, which allows both analog data processing and hardware triggering of the cameras, was used. A thermocouple was attached to the back of the specimen to monitor self-heating of the samples. Where possible, the load frequency of the test was set at 3 Hz. If it was noted that the temperature, compared to room temperature, increased by more than 20 degrees Celsius, the fatigue frequency for subsequent tests under the same loading conditions was reduced to fall below this limit.

The speckle images taken during loading of the specimen were analyzed using Vic-2D by Correlated Solutions. Lens distortions were corrected by performing a rigid body motion of a speckle pattern in the field of view together with the inverse mapping technique. In terms of subset, the software suggested size (typically around 30-50 pixels), based on the speckle pattern and image resolution, was used. Pixel distribution was analyzed using Gaussian subset weights with 6-tap spline interpolation. These typically provide a good combination and balance between spatial and displacement resolution, accuracy and correlation time. As correlation criterion, the normalized sum of squared differences was used. The consistency threshold, confidence margin and matchability threshold were kept at the default values of 0.02, 0.05 and 0.1, respectively. To process the strain field, a filter size of 15 was used where the Lagrangian strain tensor was requested.

Although the gauge length for the specimens was 25 mm, FE analysis confirmed that this gauge length was not sufficiently long to produce a true uniaxial compression in the laminate with layup $[\#(+45/-45)]_{24}$. This can also be seen in the DIC strain field measured for such sample, see Figure 4, where a diamond shape appears. Nevertheless, in order to prevent premature buckling due to fatigue degradation of the layup, the gauge length of 25 mm was kept.

Figure 4 also shows the placement of virtual strain gauges in the strain field.

3. Fatigue test results

The specimens were tested under multiple stress levels for the stress ratios $R = 10$ and $R = -1$. An overview of the tests is shown in Figure 5, which shows the strength-life data of the specimens tested. The figures show a good distribution of the experimental data for the load levels tested. Also, note that the life for $R = -1$ is, as expected, lower than the life for $R = 10$ at equivalent load levels. In the next sections the measured behaviour in terms of stiffness, permanent strain evolution and shape of the hysteresis cycles are discussed for the tests in general. The test data for each individual test can be provided upon request.

3.1. Hysteresis behaviour and damage observations

Figure 6 and 7 show representative hysteresis loops for both laminates at stress ratio $R = 10$ for a high and a low stress level. For the laminate $[\#(0/90)]_{24}$ it is seen that both at the low, Figure 6a, and high stress level, Figure 6b, the hysteresis loops show an initial quasi-linear behaviour with a moderate stiffness drop and energy dissipation towards the end-of-life.

The quasi-linear behaviour can be attributed to the fact that the fibers in the warp yarns are aligned with the loading direction. The non-linear behaviour is primarily visible for the high stress level as shown in Figure 6b. Remark that, since the same strain level is retrieved when unloading, there is no observable evolution of permanent strain. This indicates that the small curvature of the loop, and its accompanying energy dissipation, should be attributed to a reversible damage phenomenon. Inspection of the images from the side camera reveals that, already early in the fatigue life, the outer plies of the laminate show small ply delaminations. These delaminations gradually grow and multiply over time and then open when load is increasing and close again upon unloading. It is noted that the growth of damage, between measurement instances, is accompanied by a stiffness drop.

For the laminate $[\#(+45/-45)]_{24}$, thanks to the usage of DIC, the data can be processed into shear stress-strain hysteresis loops, Figure 7, according to the procedure given in ASTM D3518 [2]. Compared to the laminate $[\#(0/90)]_{24}$ very different behaviour is observed. A small amount of hysteresis is seen for the low load level accompanied by a 2% to 3% permanent shear strain deformation, Figure 7a. For the high load level, Figure 7b, the energy dissipated in the hysteresis loop is significant. Next to this, it is seen that the material state changed fast as for the same recording time, subsequent hysteresis loops show a significant evolution of permanent shear strain. The magnitude of the permanent strain is also larger, up to 10% is noted for this dataset.

Compared to the hysteresis loops for the laminate $[\#(0/90)]_{24}$ the hysteresis loops for laminate $[\#(+45/-45)]_{24}$ show a significant increase of energy dissipation and evolution of permanent strain. Inspection of the samples from the side, however, does not show significant delamination of the outer plies. The hysteresis behaviour of the $[\#(+45/-45)]_{24}$ laminate is thus caused by another phenomenon than delamination. Considering the large accumulation of permanent strain it is hypothesised that non-reversible phenomena are the primary source of stiffness degradation and permanent strain evolution. Possible candidates are abundant. Composites can exhibit creep, viscoplasticity of the matrix, diffuse fiber interface damage, matrix cracking, permanent shear strain evolution, fiber

interlocking and friction between detached fiber and matrix surfaces. It is likely that a combination of all fracture mechanisms is responsible for the hysteresis behaviour. The detailed identification of fracture mechanisms is, however, out of the scope of this paper.

Figure 8 shows representative hysteresis loops for the laminate $[\#(0/90)]_{24}$ at stress ratio $R = -1$. The hysteresis loops are quasi-linear for the first cycles. Towards the end of life, a small stiffness degradation is seen together with some energy dissipation and slight curving of the stress-strain response. These observations are similar as for the stress ratio $R = 10$. Delaminations of the outer plies occur for this load scenario as well, however they developed faster and in a more severe fashion than for $R = 10$. The amount of delamination damage, among the specimens subjected to the same load conditions, also shows larger variability.

Figure 9 shows the hysteresis behaviour for $R = -1$ for the laminate $[\#(+45/-45)]_{24}$. Similar to the laminate for $R = 10$, clear hysteresis behaviour accompanied with significant energy dissipation is observed. Comparing Figure 9a and Figure 9b it is seen that the amount of energy dissipated in a single cycle increases with increasing maximum load. Furthermore, the hysteresis loops seem to be point-symmetric and rotate significantly about the origin of the axis system before the specimen fails. As with the loading scenario for $R = 10$, the side camera does not show significant delamination of the outer plies. As such the same phenomena, intraply damage, can be proposed as the dominant degradation mechanism.

It is clear from the above discussion on damage types and hysteresis behaviour, that the failure sequence of these woven ply laminates is very complex when compression load is involved. For this, the camera setup, where the side of the sample is simultaneously interrogated with the front, is very valuable for identifying damage types, and for allowing measurement of complete hysteresis loops while fatigue loading. In the following the stiffness evolution, calculated from the hysteresis loops, is discussed.

3.2. Stiffness and permanent strain evolution

The hysteresis loops are processed to identify the stiffness loss and permanent strain deformation of the samples. In this study the stiffness of a sample at a given cycle is the so-called "dynamic" stiffness, e.g. the stiffness derived from the slope between the minimum and maximum stress level of the hysteresis loop. The permanent strain is defined as the crossing of the straight line between the minimum and maximum load with the abscissa. Both definitions are shown graphically for $R \geq 0$ in Figure 10a. Figure 10b shows the same definition for $R < 0$. Note that, in the latter, a definition of permanent strain cannot be clearly defined.

Figure 11 shows a comparison of the stiffness evolution of the laminate $[\#(0/90)]_{24}$ for the stress ratios $R = 10$ and $R = -1$ at multiple stress levels. For clarity, only one experimental curve is shown for each maximum load. As already observed from the hysteresis loops, the longitudinal stiffness does not significantly change for any stress level. There is an exception for the stress level of 90%, where a very limited stiffness degradation is observed for $R = 10$ in Figure 11a.

It is noted that the stiffness evolution for the stress ratio $R = -1$ shows, when compared to the results for $R = 10$, larger scatter in the initial stiffness. This could be attributed to: 1) the increased variability in the occurrence of outer ply delaminations as mentioned in Section 3.1 and 2) transition problems for the test machine when it passes from the Tensile to the Compressive loading quadrant leading to temporary higher loads in the system.

Figure 12 shows the comparison of the shear stiffness evolution for the laminate $[\#(+45/-45)]_{24}$ for the stress ratios $R = 10$ and $R = -1$. Both figures show an accelerating stiffness degradation with increasing maximum stress level. Figure 12b shows the three stages of stiffness evolution with an initial sharp drop followed by a relatively constant degradation and eventually accelerated degradation towards final failure. For the stress ratio $R = 10$, Figure 12a, an initial drop is observed after which the shear stiffness seems to increase in the first 1,000-10,000 cycles. This is clearly visible for the stress levels of 60% and 70%.

The stiffness increase is unexpected because the material is expected to degrade, thus become less stiff, when subjected to repetitive loading. One might be tempted to lay the cause of the stiffness increase for the laminate $[\#(+45/-45)]_{24}$ with the multiaxial stress field in the gauge section, caused by the insufficiently large gauge length of the sample. However, the multiaxial stress state in the gauge section should only have an influence on the magnitude and degradation rate of the stiffness. In fact, one would expect that the material degrades faster due to the occurrence and interaction of damage in multiple directions simultaneously. Consequently, an increase in the measured stiffness cannot be solely explained by the presence of a multiaxial stress state and further investigation is needed to reveal the true source of the phenomenon. This investigation, in the form of a post-mortem inspection of the samples and FE simulation, is shown in the next sections.

3.3. Tab debond size and stiffness increase

The usual fractographic post-mortem inspection of samples is done through investigation of the fracture zone using light or scanning electron microscopy. In this case, however, it was noted that during testing black powder debris had formed around the tabbed areas and clamps. Since the adhesive has a black colour the post-mortem inspection was directed towards the tabbed zone to inspect the state of the adhesive between the tab and coupon. To this end the samples were polished on the sides and inspected with light microscopy.

The microscopic investigation revealed that, although the tabs did not fully detach from the sample, the adhesive between tabs and coupon had significantly degraded starting from the free end located near the gauge section. The degradation is not only seen for the layup $[\#(+45/-45)]_{24}$ but also for the layup $[\#(0/90)]_{24}$. Figure 13 shows a typical image of the tabbed region near the gauge section.

To investigate the full extent of the debond, the tabs are mechanically removed from the specimens using a wedge. After removal, the shape and size of the debond zone are measured. Figure 14 shows the three shapes observed from the removal of the tabs: a "Straight" shape, mainly observed for the laminates with layup $[\#(0/90)]_{24}$, a "V-shape", mainly observed for the laminates with layup $[\#(+45/-45)]_{24}$ and an "Undefined" shape that occurred in a few outliers.

The shape of the debond identified for each sample and their accompanying mean debond area (mean between 4 tabs on one coupon) is shown in Figure 15. Figure 15a confirms the earlier statement that Straight and V-shapes are mostly observed for layups $[\#(0/90)]_{24}$ and $[\#(+45/-45)]_{24}$, respectively. To allow a quantified comparison, the stiffness increase, defined by the difference between the lowest initial and subsequent highest measured stiffness is determined for all samples and layups, and shown in Figure 16. In the Figure, datapoints without coloured square indicated no measurable stiffness increase. The latter is primarily seen at high load levels. For the layup $[\#(0/90)]_{24}$, Figure 16a, the stiffness increase is limited to less than 5%. For the layup $[\#(+45/-45)]_{24}$ a measured stiffness

increase of up to 17% is measured for the case of $R = 10$ and a load level of 70%. Note also that CC fatigue loading prominently results in a higher stiffness increase than corresponding experiments for TC loading.

A number of additional observations are drawn. First, it appears that the longer the specimen life, the larger the debond area. Thus, it seems that the debond zone developed during the entire lifetime of the sample. Second, it is observed that the debond area is larger for the layup $[\#(0/90)]_{24}$ compared to the layup $[\#(+45/-45)]_{24}$. In contrast, the stiffness increase is larger for the laminate $[\#(+45/-45)]_{24}$. Hence, there is no direct relationship between the size of the debond and the stiffness increase. However, consider that the stress state in the gauge section of the laminate with layup $[\#(0/90)]_{24}$ is quasi-uniform. Therefore, a change in the boundary conditions at the edge of the gauge section should, since tab debonding releases local restrictions, have a minimal influence on the stress state. This is different for the layup $[\#(+45/-45)]_{24}$. Here the stress state in the gauge section is non-uniform due to the restrictions imposed by the clamping of the tabs. If this restriction is relaxed, the stress state in the gauge section could change, leading to a different reading of strain, and consequently stiffness. This second observation could thus support the hypothesis that the measured stiffness is caused by a combined non-uniform stress state with tab debonding.

From the above investigation it is clear that stiffness increase measurement is not a single occurrence but repeated for several loading scenarios. Particularly, the fact that the layup $[\#(+45/-45)]_{24}$ is affected also indicates that a multiaxial stress state in combination with changing boundary conditions have a role in this. In the following section this role is illustrated by modelling the mechanism involved using FE analysis.

4. FE simulation of tab debonding

To investigate the influence of tab debonding, the coupons are numerically modelled using a commercial Finite Element (FE) software. The investigation in this work is limited to showing the effect of tab debonding on the stress-strain distribution and measurement in the gauge section. The authors do not aim to model the behaviour of the coupon in a complete fatigue FE simulation. The latter would not only require a fatigue damage model of the woven Carbon/Epoxy material but also knowledge about the debond rate of the tab adhesive in fatigue loading in at least mode II and mode III fracture modes. Additionally, such an analysis would require extensive computational resources for which the use is not justified considering the limited knowledge of the material behaviour and the fact that it is only required to reveal the mechanism, rather than exactly replicate the experiments.

Following the previous argumentation it is sufficient to perform a quasi-static Loading-Unloading (LU) simulation. In this simulation, the specimen is first loaded (in compression) while the tabs are allowed to debond until the debond size is large. Next, the coupon is unloaded to identify the effect of the debond on the stress/strain distribution.

4.1. Model overview

An overview of the coupon, tabs and clamp abstraction can be seen in Figure 17. The dimensions of the model are equal to the real coupon dimensions in millimeters. The Figure clearly shows the composite coupon material with tabs added on each end. Tabs and coupon are modelled as separate entities which are connected to one-another using a general contact definition between tab surface and coupon surface. The properties of the contact definition between tab and coupon are shown in Table 1. The maximum nominal stress criterion is used to model damage initiation.

Damage evolution is modelled using the BK-criterion [10] (Benzeggagh-Kenane) built-in in the software. The values for damage initiation are taken from the Loctite 480 datasheet [11]. The properties for the damage evolution are not available from the datasheet and are therefore assumed to be equal to interlaminar interface energy for a typical Carbon/Epoxy laminate [12]. Last but not least, damage stabilization with a viscosity coefficient is introduced. This is necessary to aid convergence of the solution when damage develops (quasi-static solver is implicit).

Concerning material behaviour, the tabs are assigned an isotropic linear elastic material model with typical material properties for aluminium, Table 2. The composite parts are assigned a phenomenological material model for woven materials developed by Hochard and Miot [13]. The material model provides a global behaviour in terms of permanent strain evolution and stiffness degradation due to internal damage such as diffuse debonding and microcracking. The details of the model are provided in [13]. The material parameters are determined from static tensile testing according to the procedure in [14] and [15]. The values are shown in Table 3. Note that a significant share of the parameters needed to be estimated from literature. The parameters determined with confidence mainly consider the behaviour of the plies in the shear direction.

The clamping action of the clamps on the tab surface is applied using boundary conditions in the form of constraint equations. First, the clamp and tab surface are assumed to stay in full contact and do not slip. Second, the hardened steel clamp is assumed to be infinitely stiff compared to the aluminium tab. In this way, the surface of the tabs can not be strained in the xy plane. To achieve a uniform motion of the tab surfaces in the x and y direction, use is made of constraint equations and reference points as follows:

$$\begin{cases} u_{surf,i} - u_{RP,k} = 0 \quad i = 1,2; k = 1 \quad i = 3,4; k = 2 \\ v_{surf,i} - v_{RP,k} = 0 \quad i = 1,2; k = 1 \quad i = 3,4; k = 2 \end{cases} \tag{1}$$

where u and v are displacements in the $x-$ and $y-$ direction respectively. $surf, i$ refers to a tab surface i and RP, k is reference point k. The denotations are illustrated for both tabbed sides in Figure 18.

Together with the movement in $x-$, $y-$ direction the clamps execute a clamping pressure force on the tabs. For this, it is important to realize that the clamp surface will always stay parallel to its initial position. The entire surface of the tab must thus remain parallel to its initial position while the clamping pressure is applied. The clamping action is achieved using an additional reference point and restricting movement in z-direction as follows:

$$\begin{cases} w_{surf,i} - w_{RP,k} = 0 \quad i = 1; k = 1 \quad i = 3; k = 2 \\ w_{surf,i} - w_{RP,k} = 0 \quad i = 2; k = 3 \quad i = k = 4 \end{cases} \tag{2}$$

where w is the movement in the $z-$direction.

The clamping force is then applied to RP,3 and RP,4. With respect to this force, note that the experimental pressure on the hydraulic line of the grips is related to, but not equal to the actual force exerted by the clamped surface. This because a series of wedges is used to convert the pressure force to a gripping force. The manufacturer of the grips did not provide information regarding this relation and therefore the clamping pressure on the side of the tabs in the simulation was set to the estimated value of 10 MPa. Regardless of whether this value is correct, for the simulations in this study the size of the clamp pressure is not expected to have a big influence because 1) the contact between

debonded surfaces of tab and specimen is frictionless and 2) the material model used for the composite material does not respond to out-of-plane loads.

The compressive (or tensile) movement action of the actuator is achieved by fixing RP,2 in its position and placing force or displacement boundary conditions on RP,1 as illustrated in Figure 18.

The results of the FE analysis are processed into global stress-strain curves in a similar way as was done for the experiments. The global reaction force is taken from the RP,1 and the strain is obtained from the displacement of the nodes in the gauge length on the sample surface. 4 nodes are chosen: 2 aligned with the main loading axis, to obtain the longitudinal strain, and 2 perpendicular to the loading axis, to obtain the transverse strain. Care is taken such that the position of the nodes selected is the same as the position of the virtual strain gauges which were used for the DIC analysis of the experimental data, see Figure 4. In this way the global stress-strain curves of both the experiment and simulation can be correctly compared.

Before the model is used to investigate tab debonding, a mesh convergence study is performed to determine the maximum converged mesh size. For this purpose the debonding of the tabs is disabled (the tabs stay attached during the entire analysis) and the global stress-strain curve is compared for increasingly finer mesh sizes. This showed that a mesh size of 1.67 mm is sufficiently small to obtain converged global stress-strain behaviour.

4.2. Simulation results

Two simulations are performed: 1) a simulation where tab debonding is not activated and the sample is simply compressed, 2) a simulation where tab debonding is allowed but the load cycle is changed such that after first debonding the coupon is unloaded to zero stress (e.g. Loading-Unloading, LU scheme). The latter is done to identify possible changes in the global stiffness of the specimen. The resulting global stress-strain behaviour for both simulations is shown in Figure 19. The chronological evolution of stress and strain is shown with arrows.

For the coupon with tab debonding the global stress-strain behaviour initially shows the same behaviour as the coupon without debonding. At a stress of about 32 MPa the curve starts to show a lower strain for approximately the same load. Next, when unloading one can clearly see that the stiffness of the coupon has increased (17%) compared to the initial situation where no debonding is present. Inspection of the simulation reveals that the reduction in longitudinal strain is accompanied by a large growth in the size of the debond between tabs and coupon. To illustrate, Figure 20 shows the amount of debonding at debond onset, t=0.20 and after development of a large debond as shown in Figure 20a and Figure 20b respectively. The reference positions in the global stress-strain curve of both times are shown in Figure 19 by the red and black asterisk. t=0.20 is chosen as a reference time because the debond initiates, t=0.75 is subsequently selected because the load on the coupon is closest to the load applied at t=0.20. Note that the shape of the debond shows a V-shape. This agrees with the V-shaped transition zone observed in the experimental program for the layup $[\#(+45/-45)]_{24}$, see Figure 14a.

The stress fields of the in-plane ply shear stress for the selected instants are shown in Figure 21 with and without tabs (to show the stress distribution in the composite below the tabs). Figure 21a confirms the existence of a multiaxial stress state before debonding. Note that the shear stress beneath the tabbed region drops to zero, Figure 21c. This is in contrast with the situation where the tabs have partially debonded, Figure 21b. Here the stress field is clearly more

uniform and the Carbon/Epoxy underneath the debonded tabbed region is now subjected to significant stress levels, Figure 21d.

These observations reveal the mechanism behind the apparent stiffness increase seen in the coupons. The debonding of the tabs effectively increases the size of the gauge section underneath the tabbed region and inside the clamps. The larger gauge section allows the load, introduced by the clamps, to redistribute more evenly over the larger gauge section which results in a more uniform distribution of the stress/strain field observed by the DIC camera. This results in a gradual apparent increase in stiffness of the sample.

In fact, the initial non-uniform stress distribution, due to the short gauge length, also results in a false measurement of the stiffness of the coupon. This is easily proven by comparing the global stress-strain behaviour of a coupon with a long and short gauge length as shown in Figure 22. Clearly, the coupon with a long gauge section, where a uniform stress distribution is present from the start, shows the stiffer behaviour.

The observations done from the quasi-static simulation of the observed damage mechanisms can now be connected to the observations from the fatigue experiments. During fatigue loading it is well known that damage mechanisms develop at a much slower rate when compared to static loading. As such it is hypothesized that in the first 10,000 cycles of the experiment the bond between tab and coupon deteriorates much slower than shown in the quasi-static simulation. The slow deterioration results in a slow redistribution of the stress field which consequently shows as an apparent increase of global stiffness of the coupon. The apparent stiffness increase halts when the debond is large enough to produce a uniaxial stress state in the gauge section after which the distribution, provided that the maximum load stays the same, does not change anymore under influence of the tabs. As a result, what follows is the natural reduction of the specimen stiffness due to matrix cracking and delamination.

Note that this hypothesis is only valid when the stiffness reduction of the Carbon/Epoxy weave (due to fatigue) is slower than the stiffness increase by tab debonding. Since it is known that degradation of the material is influenced by the fatigue load, it is therefore conceivable that the stiffness increase is less prominent at higher loads. The occurrence of such a case would be more dangerous because the experimental data would show no indication of the redistribution of stress and strain. Therefore, for future tests on short gauge length coupons, it is advised to confirm always whether tab debonding has occurred to identify changes in the boundary conditions on the gauge section.

5. Discussion and conclusion

In this work the results of an experimental study on the CC and TC behaviour of woven Carbon/Epoxy plies in ply normal and shear direction are presented. Short gauge length specimens with layups $[\#(0/90)]_{24}$ and $[\#(+45/-45)]_{24}$ are tested in a uniaxial servohydraulic tensile machine under different load levels and stress ratios. The strain on the surface is measured using a novel DIC camera setup. One camera is pointed to the front and one to the side. This allows to determine the stress-strain hysteresis loops of the coupons and detect essential damage mechanisms, such as ply delamination, during fatigue testing.

For most tests the stiffness evolution shows an acceptable behaviour up to failure of the specimens. For the layup $[\#(+45/-45)]_{24}$ and $R = 10$, however, a notable increase in stiffness in the first 1,000 - 10,000 cycles is found. The cause of the latter is the interaction between a multiaxial stress state and a change of boundary conditions induced by

the clamps and the short gauge length of the sample. In fact, post-mortem inspection and subsequent FE simulation shows that the adhesive between the tab and coupon has deteriorated over time. The mechanism behind the stiffness increase is identified as a transition from a multiaxial stress state to a uniaxial stress state from the increase in gauge length due to partial debonding of the tabs.

Although in this work a focus is laid on compression fatigue, the same phenomena can occur in tension fatigue if the size of the gauge section is not sufficiently large to produce a uniform stress field, or if the measurement of strain on the sample was done near the clamped region.

Hereby an alternative explanation for apparent stiffness increase in fatigue loading than the common explanation of fiber reorientation [3, 4, 6] is given. The tab debond process can significantly change the stress/strain state in the gauge section of a short gauge length coupon. In this case, the test data was processed as if the stress state was uniaxial. Therefore, the data in Figure 12 is corrupt at least until the peak stiffness. After that the increased gauge section due to the tab debond was sufficiently large such that it did not influence the stress distribution anymore. Note, however, that the validity of the test data is largely dependent on the adhesive used. Depending on the quality of the adhesive, the scenario can be different. For example, it is possible that the stiffness increase by degradation of the tab bond is countered fully by the decrease in stiffness of the material. In that case, the measured stiffness would remain constant until failure. Even worse, it is possible that the stiffness increase by bond degradation is slower than the stiffness decrease of the material. Then the measurement would show a regular gradual degradation of the stiffness which is, nonetheless, equally invalid because the degradation would appear slower than in reality.

Remark that this stiffness increase only shows in graphs where a logarithmic scale is used for the axis depicting the number of cycles to failure. When a linear scale for the horizontal axis is used the initial 10,000 cycles, being 1% of the number of cycles at run-out (1,000,000) are quasi-invisible on the chart. This is shown in Figure 23 for laminate $[\#(+45/-45)]_{24}$ with $R = 10$ and $\sigma_{xx,max} = 94MPa$. Since most authors [16, 17, 18, 19, 20, 21, 22] use the linear scale it is therefore possible that stiffness increase has remained undetected in a significant amount of studies.

It is emphasized, again, that the issue with boundary conditions presented here is only present if the gauge length is too short to give a quasi-uniaxial stress state in the gauge section. Laminates with a low Poisson's ratio should thus not suffer significantly from this phenomenon. Alternatively, compression testing of off-axis and angle-ply laminates is highly sensitive to clamping effects and care should be taken of the stress state in the gauge section.

Although in this work also a non-uniform stress state is present, recall that it was known and acknowledged beforehand. Unfortunately, the existence of the latter was unavoidable because the gauge length needed to be shortened to avoid buckling. For future short gauge length uniaxial compression tests, it is extremely important to develop new specimen designs which produce a uniaxial stress state in the gauge section while avoiding buckling.

6. Acknowledgement

The work leading to this publication has been funded by the SBO project M3Strength (Grant no. 130546), which fits in the Macro- ModelMat (M3) research program funded by SIM (Strategic Initiative Materials in Flanders) and VLAIO (Flanders Innovation & Entrepreneurship Agency).

References

[1] ASTM International, D3410M - Standard Test Method for Compressive Properties of Polymer Matrix Composite Materials with Unsupported Gage Section by Shear Loading, Annual Book of ASTM Standards 15.03 (Reapproved 2008) (2003) 1–16. doi:10.1520/D3410.

[2] D 3518, Standard Test Method for In-Plane Shear Response of Polymer Matrix Composite Materials by Tensile Test of a [+-45] Laminate, Annual Book of ASTM Standards 94 (Reapproved) (2007) 1–7. doi:10.1520/D3518.

[3] M. M. Shokrieh, Progressive Fatigue Damage Modeling of Composite Materials, Ph.D. thesis, McGill University, Montréal Canada (1996).

[4] M. M. Shokrieh, L. B. Lessard, Progressive Fatigue Damage Modeling of Composite Materials, Part I: Modeling, Journal of Composite Materials 34 (13) (2000) 1056–1080. doi:10.1177/002199830003401301.
URL http://jcm.sagepub.com/cgi/doi/10.1177/002199830003401301

[5] F. Daghia, P. Ladeveze, Identification and validation of an enhanced mesomodel for laminated composites within the WWFE-III, Journal of Composite Materials 47 (20-21) (2013) 2675–2693. doi:10.1177/0021998313494095.
URL http://jcm.sagepub.com/cgi/doi/10.1177/0021998313494095

[6] J. Brunbauer, G. Pinter, On the strain measurement and stiffness calculation of carbon fibre reinforced composites under quasi-static tensile and tension-tension fatigue loads, Polymer Testing 40 (2014) 256–264. doi:10.1016/j.polymertesting.2014.09.014.
URL http://linkinghub.elsevier.com/retrieve/pii/S0142941814002165

[7] S. Stelzer, R. Rieser, G. Pinter, DAMAGE EVOLUTION IN GLASS FIBRE REINFORCED COMPOSITES, in: ECCM17 - 17th European Conference on Composite Materials, Munich, Germany, 2016, pp. 3258–3263.

[8] S. Walraet, Compression-Compression and Tension-Compression Fatigue of Woven Carbon-Epoxy Composites, Tech. rep., Delft University of Technology (2017).

[9] ASTM, ASTMD6641: Standard Test Method for Compressive Properties of Polymer Matrix Composite Materials Using a Combined Loading Compression (CLC), Annual Book of ASTM Standards i (Clc) (2012) 1–11. doi:10.1520/D6641.

[10] M. Benzeggagh, M. Kenane, Measurement of mixed-mode delamination fracture toughness of unidirectional glass/epoxy composites with mixed-mode bending apparatus, Composites Science and Technology 56 (4) (1996) 439–449. doi:10.1016/0266-3538(96)00005-X.
URL http://www.sciencedirect.com/science/article/pii/026635389600005X

[11] Henkel, Loctite 480 Technical Data Sheet, Tech. rep. (2017).
URL http://www.henkel-adhesives.com.au/3319{_}AUE{_}HTML.htm?nodeid=8797712744449

[12] A. Arteiro, G. Catalanotti, A. Melro, P. Linde, P. Camanho, Micro-mechanical analysis of the in situ effect in polymer composite laminates, Composite Structures 116 (2014) 827–840. doi:10.1016/j.compstruct.2014.06.014.
URL http://linkinghub.elsevier.com/retrieve/pii/S0263822314002839

[13] C. Hochard, Y. Thollon, A generalized damage model for woven ply laminates under static and fatigue loading conditions, International Journal of Fatigue 32 (1) (2010) 158–165. doi:10.1016/j.ijfatigue.2009.02.016.
URL http://linkinghub.elsevier.com/retrieve/pii/S0142112309000619

[14] S. Miot, Rupture de structures composites stratifiées sous chargements statique et de fatigue, Phd thesis, Aix-Marseille Université (2009).

[15] P. Ladeveze, E. LeDantec, Damage modelling of the elementary ply for laminated composites, Composites Science and Technology 43 (3) (1992) 257–267. doi:http://dx.doi.org/10.1016/0266-3538(92)90097-M.
URL http://www.sciencedirect.com/science/article/pii/026635389290097M

[16] S. Adden, P. Horst, Stiffness degradation under fatigue in multiaxially loaded non-crimped-fabrics, International Journal of Fatigue 32 (1) (2010) 108–122. doi:10.1016/j.ijfatigue.2009.02.002.
URL http://dx.doi.org/10.1016/j.ijfatigue.2009.02.002

[17] H. Mao, S. Mahadevan, Fatigue damage modelling of composite materials, Composite Structures 58 (4) (2002) 405–410. doi:http://dx.doi.org/10.1016/S0263-8223(02)00126-5.
URL http://www.sciencedirect.com/science/article/pii/S0263822302001265

[18] A. Shirazi, A. Varvani-Farahani, A Stiffness Degradation Based Fatigue Damage Model for FRP Composites of $(0/\theta)$ Laminate Systems, Applied Composite Materials 17 (2) (2009) 137–150. doi:10.1007/s10443-009-9099-1.
URL http://link.springer.com/10.1007/s10443-009-9099-1

[19] S. M. Spearing, P. W. R. Beaumont, Fatigue damage mechanics of composite materials. I: Experimental measurement of damage and post-fatigue properties, Composites Science and Technology 44 (2) (1992) 159–168. doi:10.1016/0266-3538(92)90109-G.

[20] C. R. Kennedy, S. B. Leen, Fatigue of Glass Fibre Reinforced Polymers, in: 16Th European Conference on Composite Materials, no. June, Seville, Spain, 2014, pp. 1–8.

[21] Y. Feng, Y. He, C. Gao, T-T fatigue behaviors of composite T800/MTM46 cross-ply laminate and reliability analysis on fatigue life, Advances in Mechanical Engineering 9 (5) (2017) 1–14. doi:10.1177/1687814017704829.
URL http://journals.sagepub.com/doi/10.1177/1687814017704829

[22] T. Philippidis, A. Vassilopoulos, Fatigue of composite laminates under off-axis loading, International Journal of fatigue 21 (1999) 253–262.
URL http://www.sciencedirect.com/science/article/pii/S0142112398000735

[23] R. D. B. Sevenois, D. Garoz, F. A. Gilabert, S. W. F. Spronk, S. Fonteyn, M. Heyndrickx, L. Pyl, D. V. Hemelrijck, J. Degrieck, W. V. Paepegem, Avoiding interpenetrations and the importance of nesting in analytic geometry construction for Representative Unit Cells of woven composite laminates, Composites Science and Technology 136 (2016) 119–132. doi:10.1016/j.compscitech.2016.10.010.
URL http://linkinghub.elsevier.com/retrieve/pii/S0266353816304560

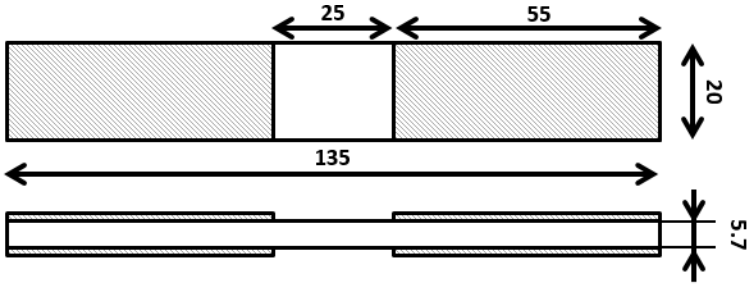

Figure 1: Specimen dimensions for CC and TC

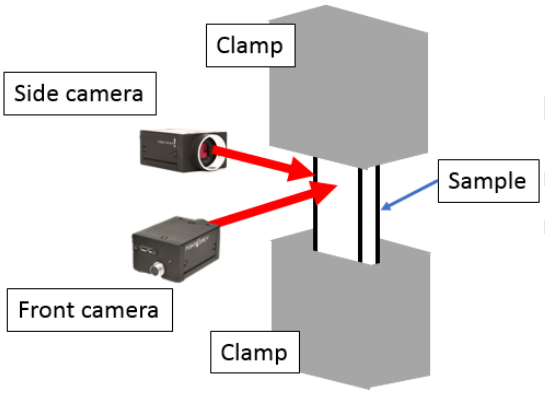

Figure 2: Test setup with one camera to front and one camera to the side

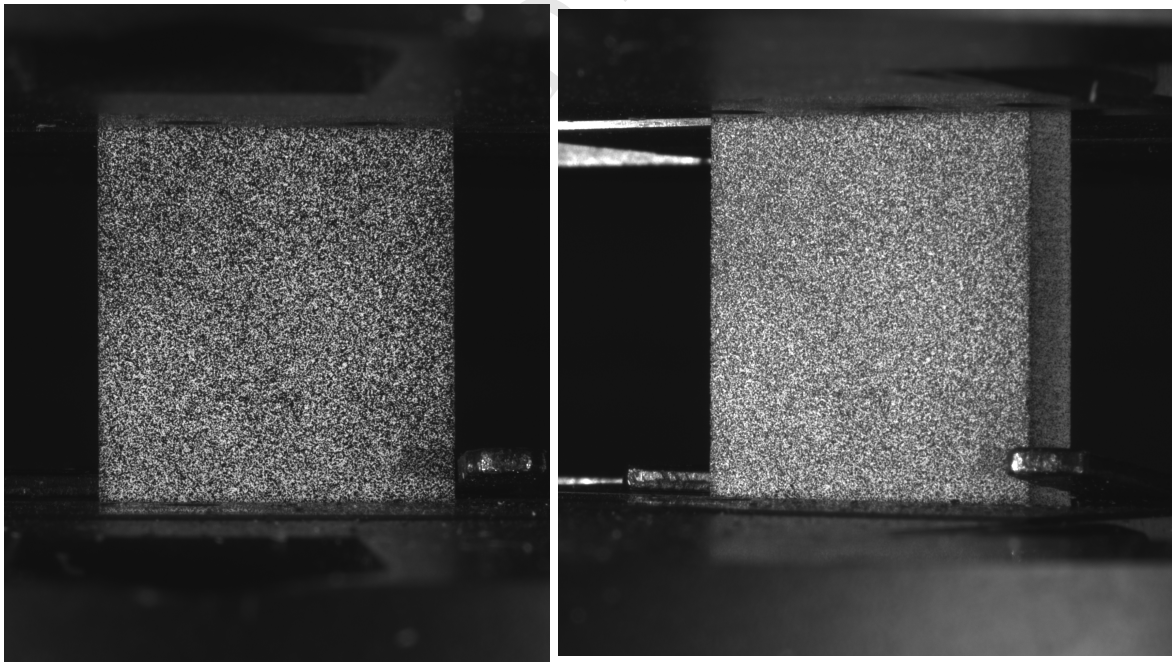

(a) Front view (b) Side view

Figure 3: Compression specimen in between clamps with speckle pattern.

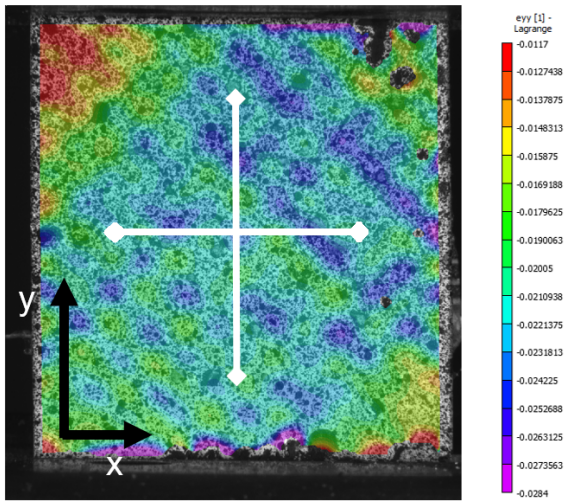

Figure 4: Vertical strain distribution from DIC. Sample 37 at 4,279 cycles with layup $[\#(+45/-45)]_{24}$ and virtual extensometer (white) (local DIC coordinate system)

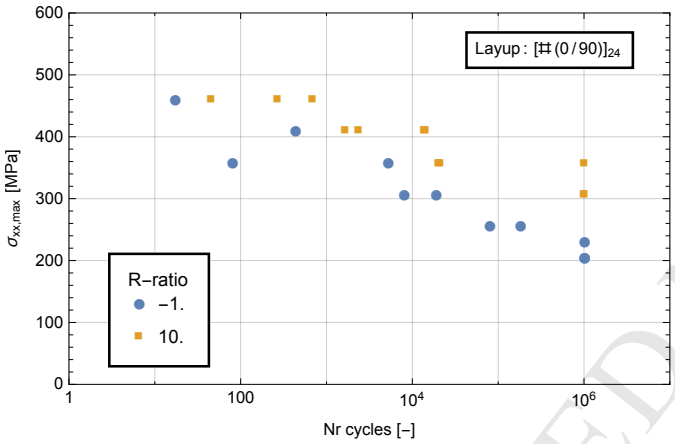

(a) Laminate $[\#(0/90)]_{24}$

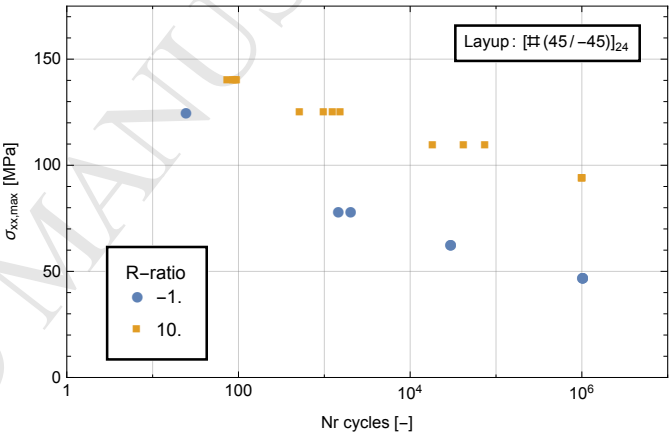

(b) Laminate $[\#(+45/-45)]_{24}$

Figure 5: Strength life data for woven Carbon/Epoxy laminates subjected to CC and TC fatigue on a linear-log scale. Datapoints at 10^6 cycles indicate run-out

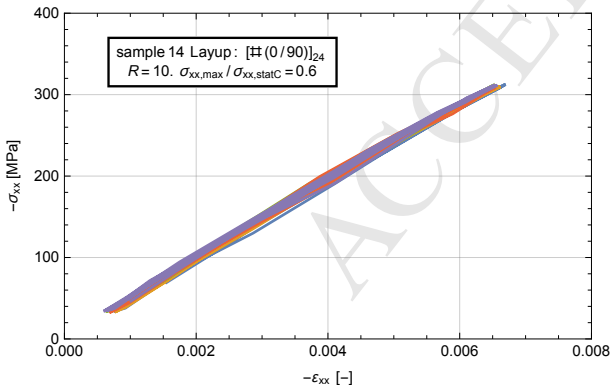

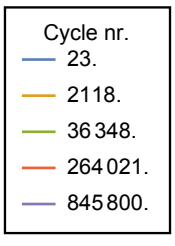

(a) Stress level 60%

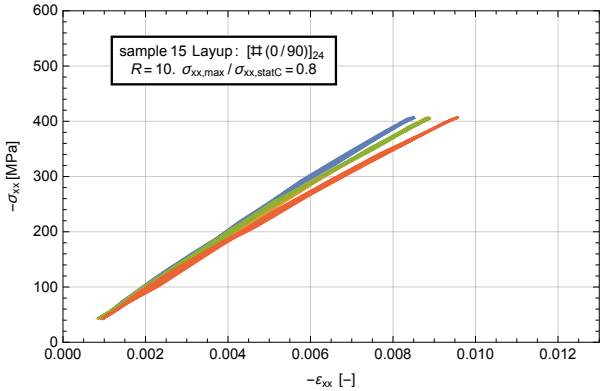

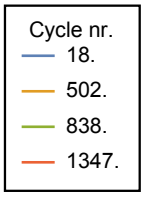

(b) Stress level 80%. Note: cycle 502 is below cycle 838

Figure 6: Representative hysteresis behaviour for laminate $[\#(0/90)]_{24}$ with stress ratio $R = 10$ at two stress levels

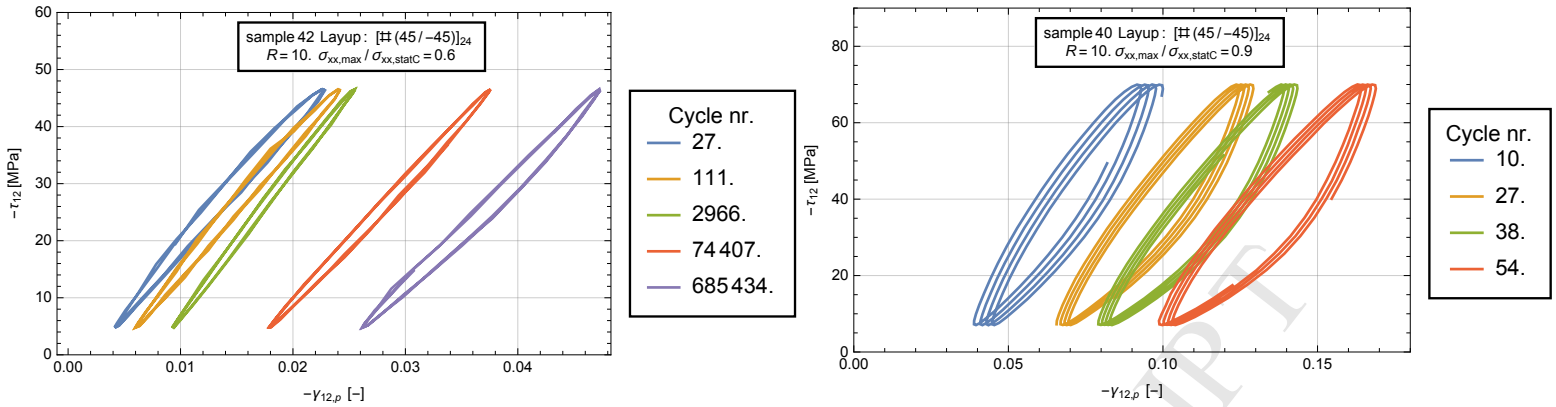

(a) Stress level 60% (b) Stress level 90%

Figure 7: Representative hysteresis behaviour for laminate $[\#(+45/-45)]_{24}$ with stress ratio $R = 10$ at two stress levels

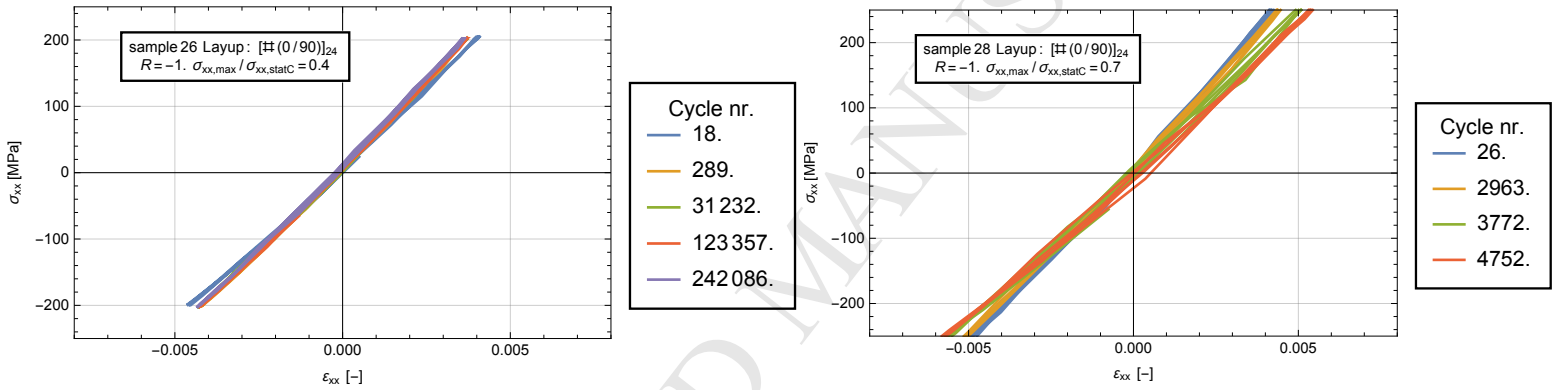

(a) Stress level 40% (b) Stress level 70%

Figure 8: Representative hysteresis behaviour for laminate $[\#(0/90)]_{24}$ with stress ratio $R = -1$ at two stress levels

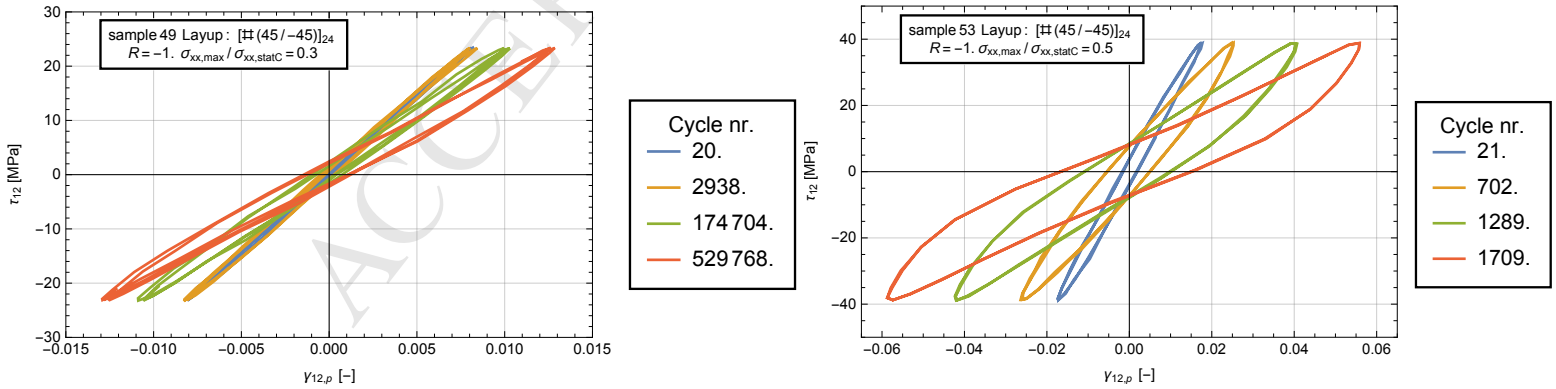

(a) Stress level 30% (b) Stress level 50%

Figure 9: Representative hysteresis behaviour for laminate $[\#(+45/-45)]_{24}$ with stress ratio $R = -1$ at two stress levels

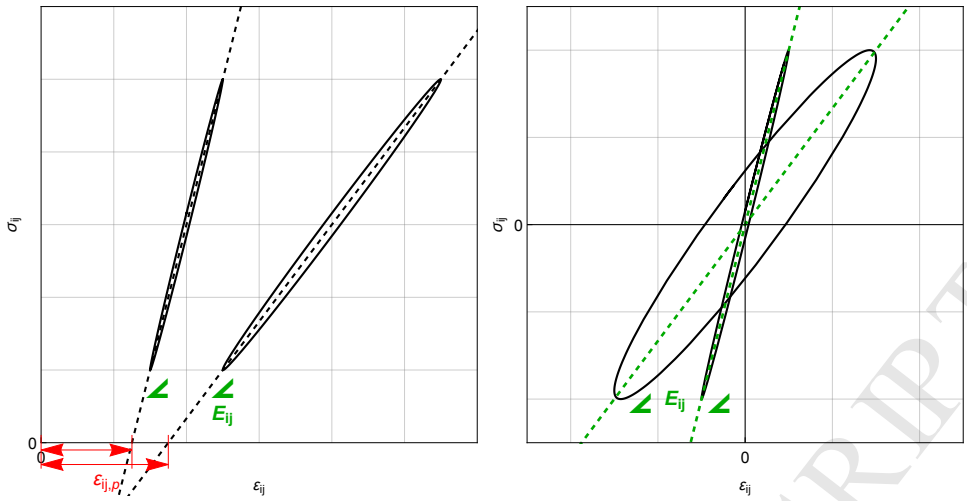

(a) $R \geq 0$ (b) $R < 0$

Figure 10: Definition of stiffness and permanent strain in CC and TC loading

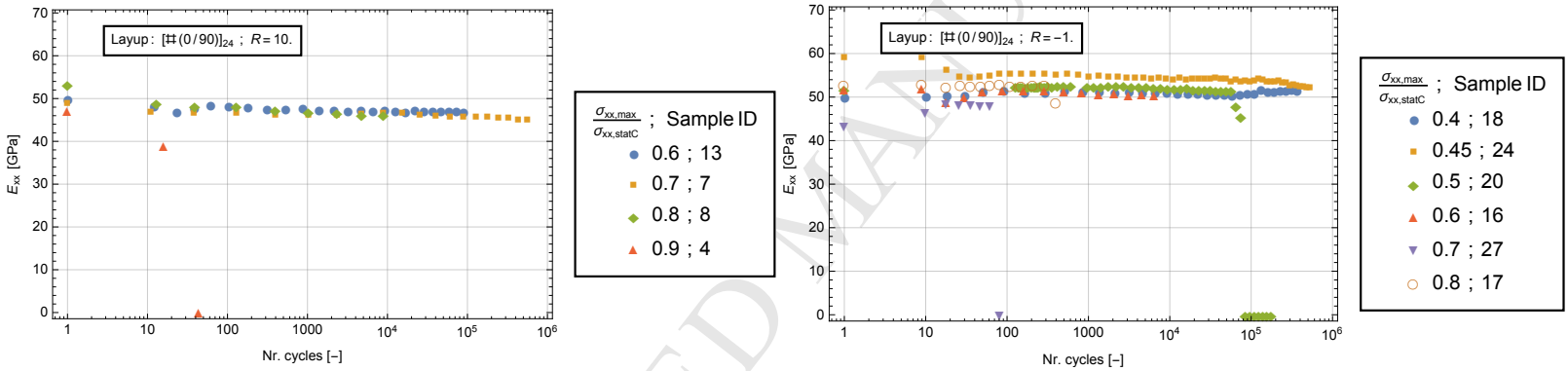

(a) Stress ratio $R = 10$ (b) Stress ratio $R = -1$

Figure 11: Representative stiffness evolution for laminate $[\#(0/90)]_{24}$ on a linear-log scale.

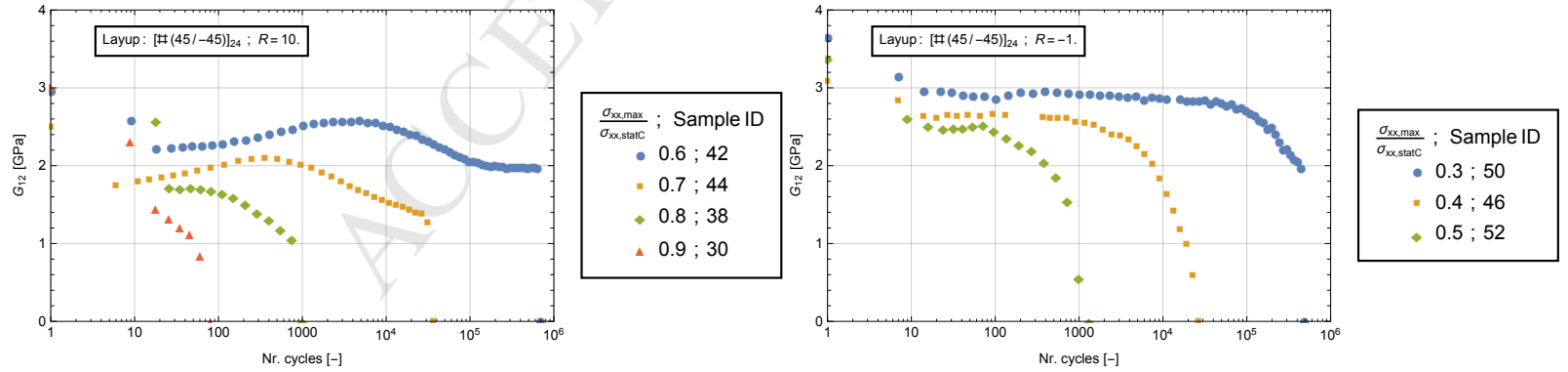

(a) Stress ratio $R = 10$ (b) Stress ratio $R = -1$

Figure 12: Representative stiffness evolution for laminate $[\#(+45/-45)]_{24}$ on a linear-log scale

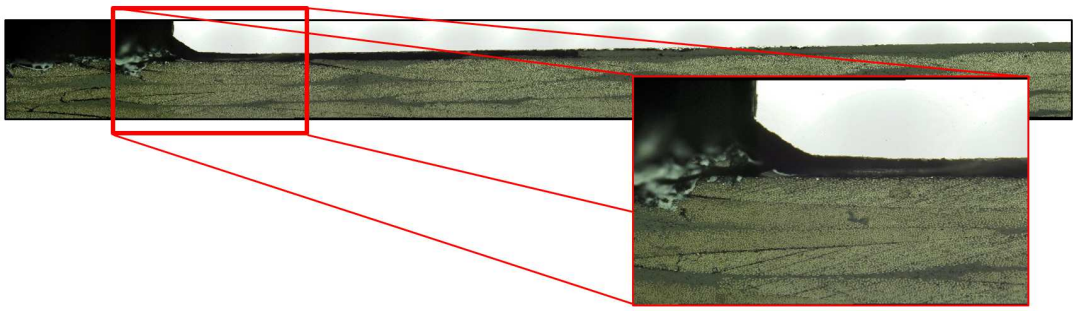

Figure 13: Microscopic view of tab debond

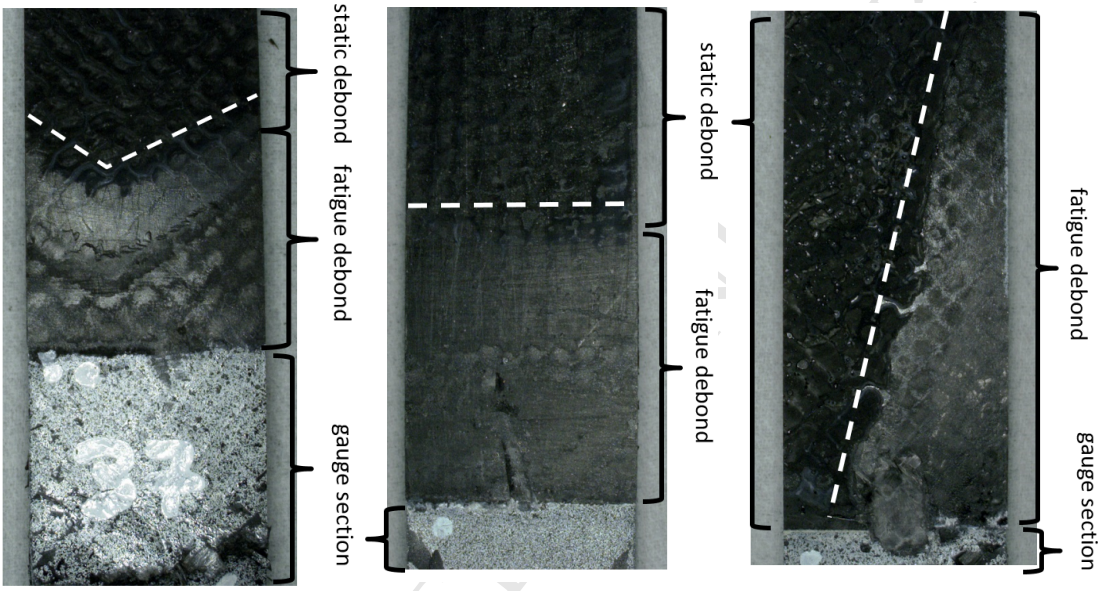

(a) V-shape (b) Straight (c) Undefined

Figure 14: Three different tab debond fracture surface shapes (indicated with white dashed line)

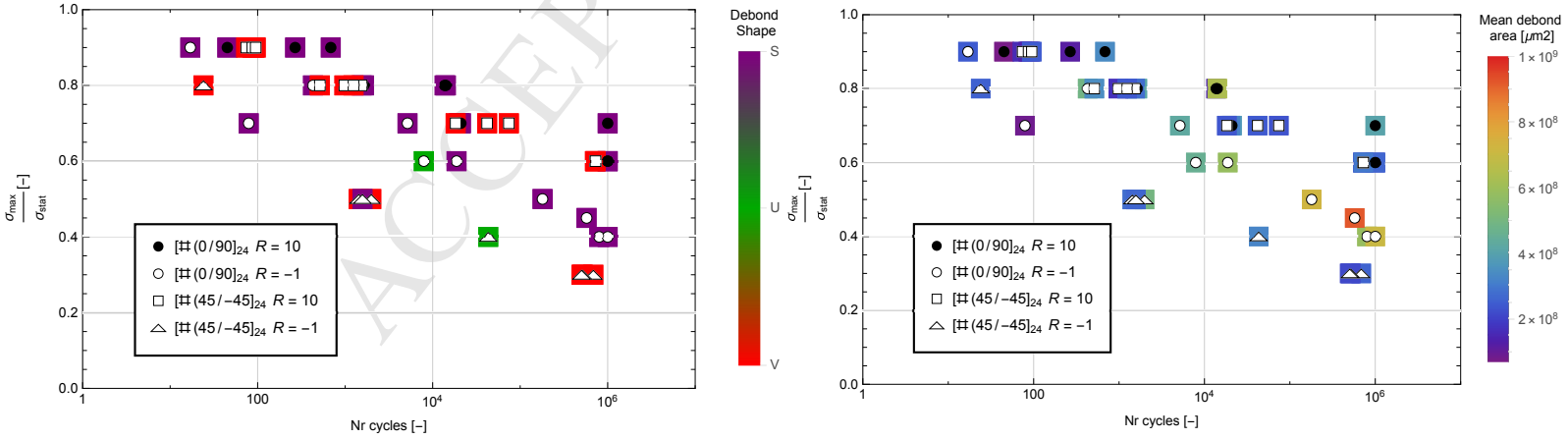

(a) Debond shape (b) Debond area

Figure 15: Shape and area of the debonded tab adhesive with respect to fatigue life on a linear-log scale

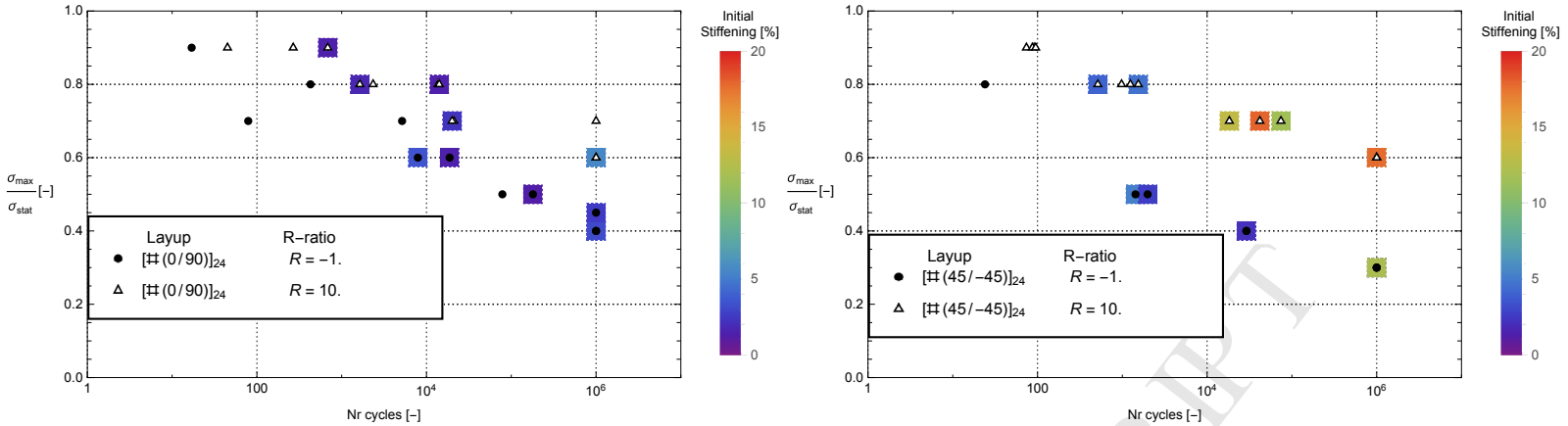

(a) Laminate $[\#(0/90)]_{24}$ (b) Laminate $[\#(+45/-45)]_{24}$

Figure 16: Measured maximum stiffness increase for plain woven Carbon/Epoxy against fatigue life on a linear-log scale

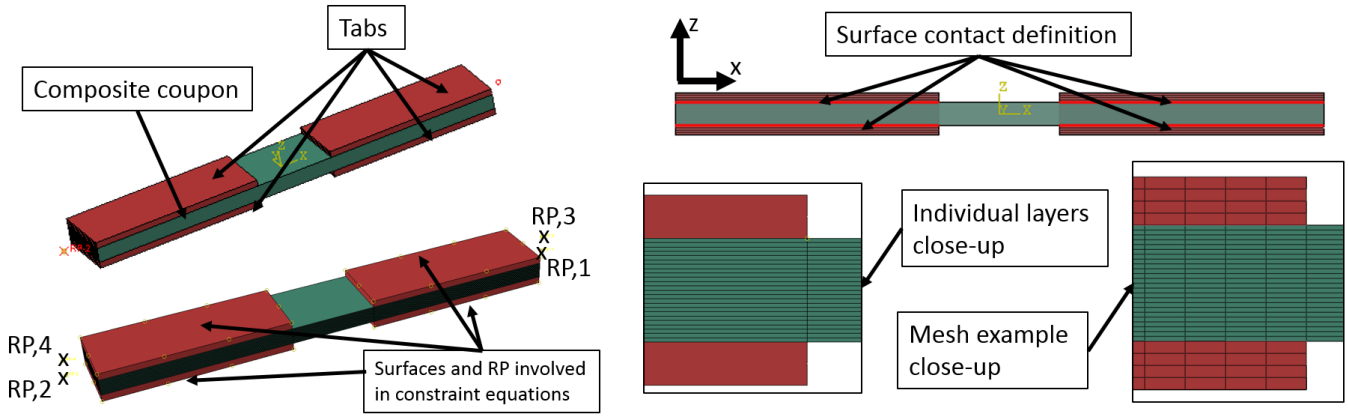

Figure 17: Model Overview

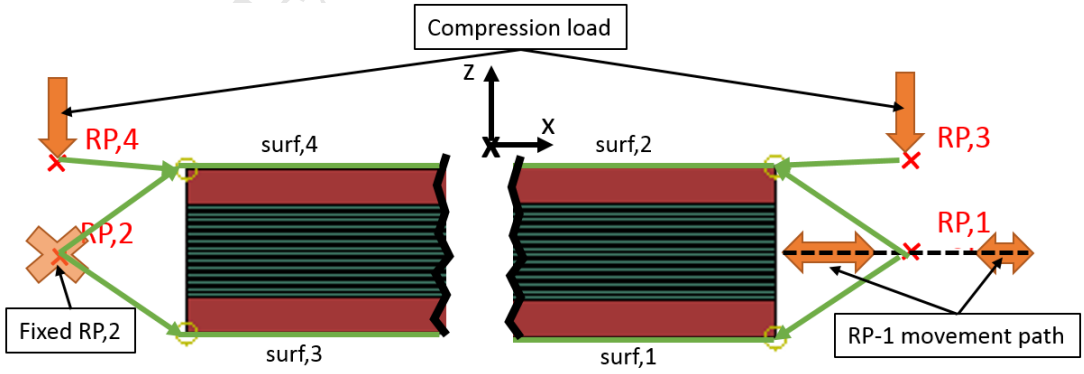

Figure 18: Clamp surface and abstractions

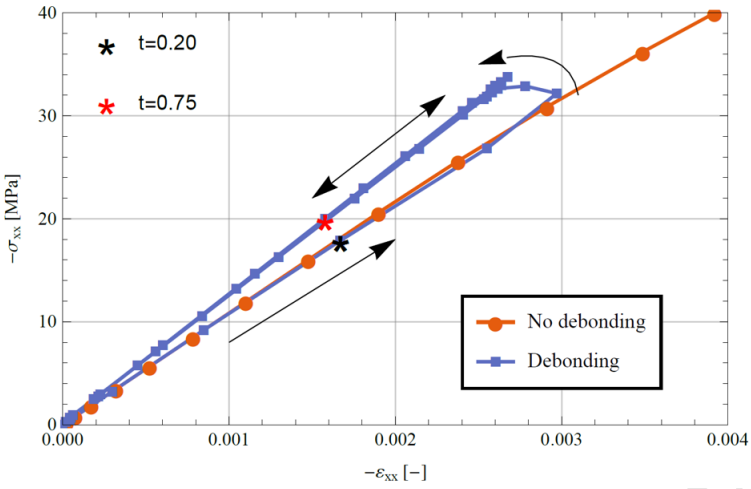

Figure 19: Global stress-strain behaviour of a specimen with layup $[\#(+45/-45)]_{24}$ with and without debonding

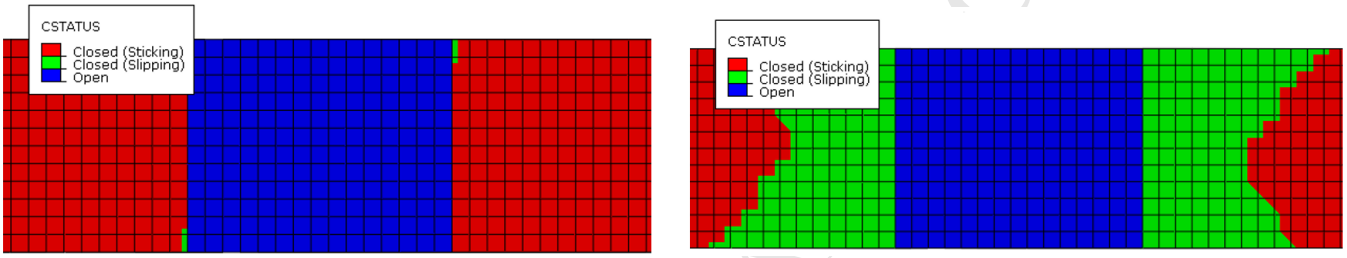

(a) $t = 0.20$

(b) $t = 0.75$

Figure 20: Size and shape of tab debond at different times

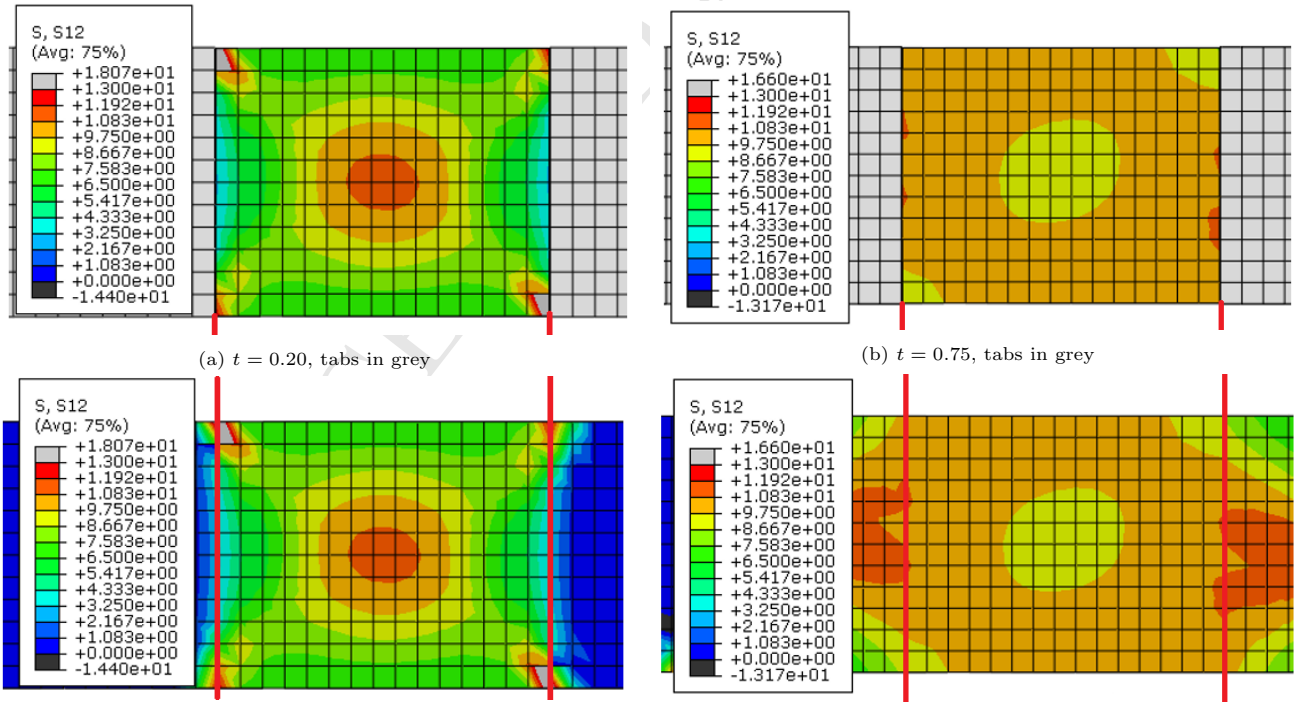

(a) $t = 0.20$, tabs in grey

(b) $t = 0.75$, tabs in grey

(c) $t = 0.20$, no tabs shown

(d) $t = 0.75$, no tabs shown

Figure 21: In-plane ply shear stress distribution at reference times with and without tabs shown

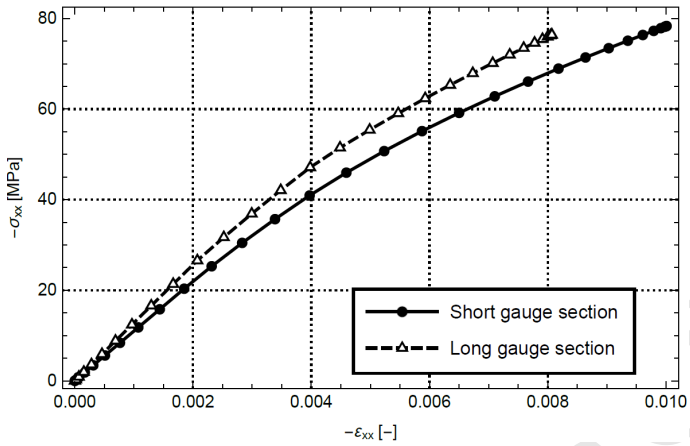

Figure 22: Global stress strain behaviour for a coupon with long and short gauge length without tab debonding

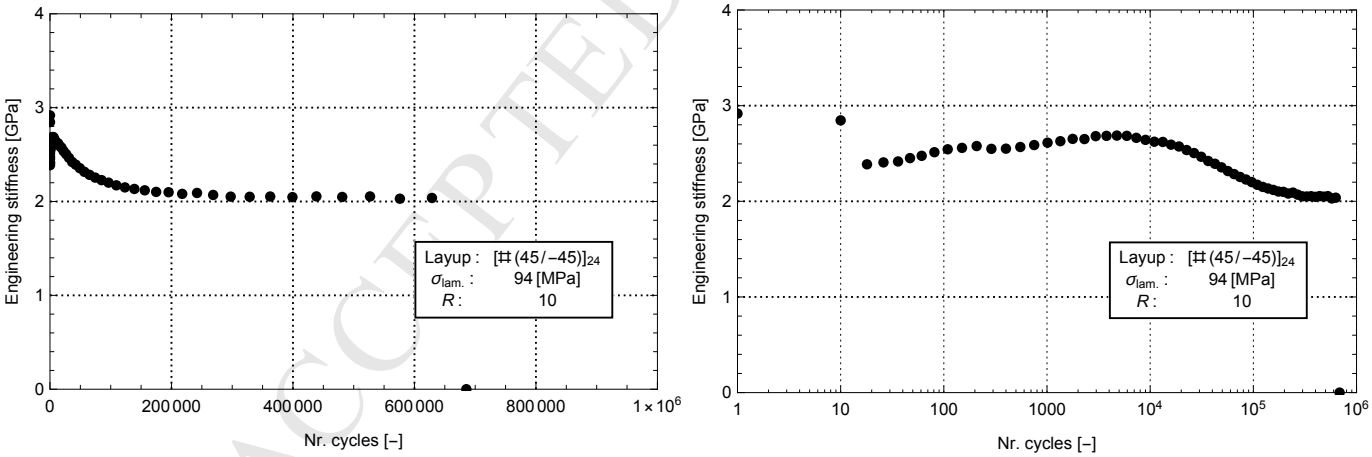

(a) Linear horizontal axis

(b) Logarithmic horizontal axis

Figure 23: Representative stiffness evolution for laminate $[\#(+45/-45)]_{24}$ with $R = 10$ with different scale for the horizontal axis

Table 1: Tab-coupon bond contact definition

Property	Value
Tangential behaviour	Frictionless
Normal behaviour	Hard contact
Cohesive behaviour	Only slave nodes initially in contact Default traction separation behaviour
Damage Initiation	Maximum nominal stress [11] $\sigma_{normal} = 10$ MPa $\tau_1 = 20$ MPa $\tau_2 = 20$ MPa
Damage Evolution	BK criterion [12] Exponential softening BK power 1.634 $G_{Ic} = 0.277$ N/mm $G_{IIc} = 0.788$ N/mm $G_{IIIc} = 0.788$ N/mm
Damage stabilization	0.0001

Table 2: Material properties for aluminium

E [GPa]	72.0
ν [−]	0.3

Table 3: Material parameters for plain woven Carbon/Epoxy with Miot-Hochard

Parameter	plain woven Carbon/Epoxy
E_{11} [GPa]	102.6*
E_{22} [GPa]	11.4*
ν_{12} [-]	0.3**
G_{12} [GPa]	3.6
h [-]	37872
R_0 [MPa]	26.7
a [-]	0.7***
m [GPa]	0.75***
b [-]	0.58
n [GPa]	0.42
Y_0 [MPa]	0.12
c[-]	-
Y_T [MPa]	7.2

*assumed $0.11E_{1,UD} = E_{2,UD}$, **estimated from [23]; *** estimated from [14].